THE BALTIC JOURNAL
OF ROAD AND BRIDGE ENGINEERING

ISSN 1822-427X print / ISSN 1822-4288 online
2014 Volume 9(3): 225–234

DETERMINING RANGES AND SPATIAL DISTRIBUTION OF ROAD FROST HEAVE BY TERRESTRIAL LASER SCANNING

Tarvo Mill[1]✉, Artu Ellmann[2], Andrus Aavik[3], Milan Horemuz[4], Sven Sillamäe[5]

[1, 2, 3]*Dept of Road Engineering, Tallinn University of Technology, Ehitajate tee 5, 19086 Tallinn, Estonia*
[4]*Dept of Geodesy and Geoinformatics, Royal Institute of Technology, Drottning Kristinas väg 30, 10044 Stockholm, Sweden*
[5]*Faculty of Construction, Tallinn University of Applied Sciences, Pärnu mnt 62, 10135 Tallinn, Estonia*
E-mails: [1]*tarvo@tktk.ee;* [2]*artu.ellmann@ttu.ee;* [3]*andrus.aavik@ttu.ee;* [4]*milan.horemuz@abe.kth.se;* [5]*sven@tktk.ee*

Abstract. The technology of terrestrial laser scanning has evolved rapidly in recent years and it has been used in various applications, including monitoring vertical and horizontal displacements of constructions but significantly less in road frost heave assessment. Frost heave is categorised as one of the main causes of pavement surface damage in seasonal frost regions. Frost heave occurs in wintertime and in early spring at the freezing process of the ground supported structures such as roads. The major change in the structure is the increase of soil volume due to freezing of its water content. This contribution assesses vertical displacements caused by frost heave on a road using novel terrestrial laser scanning technology. The study emphasises on benefits using the technology in determining accurate magnitudes and spatial distribution of frost heave of roads. The results of case study revealed uneven spatial distribution of frost heave, which may also be an evidence of relatively poor road design quality. Therefore it is also advisable using terrestrial laser scanning in applications such as quality assessment of existing roads and in the pre-reconstruction design stage for detecting any frost heave sensitive areas in existing embankments.

Keywords: terrestrial laser scanning, levelling, frost heave, road condition measurement, pavement surface, embankment.

1. Introduction

Since the beginning of the rapid development of terrestrial laser scanning (TLS) technology in the late 1990-ies it has been used in various projects including deformation monitoring. Deformation monitoring by TLS has been reported by different authors, e.g. Tsakiri and Pfeifer (2006), Zogg and Ingensand (2008), Riveiroa *et al.* (2013). While conventional geodetic technologies focus on collecting sample data of an object with spatial resolution of some meters (depending on the object) the TLS technology captures the complete field of view with a cm range spatial resolution (e.g. Paeglītis *et al.* 2013). A thorough overview of TLS technology is presented in Reshetyuk (2009) and Vosselman and Maas (2009). The quality analysis of TLS is studied by e.g. Reshetyuk (2010) and Lichti (2010).

Occurrence of frost heave has always been a crucial indicator of the quality of the road embankment in seasonal frost regions. It is acceptable for the pavement surface of the road to rise evenly during a sustained cold period (when temperatures are mostly below freezing point) and settle during a sustained warm period. For instance, according to *Elastsete teekatendite projekteerimise juhend (Guide for the Design of Elastic Pavements)* issued by the *Estonian Road Administration* in 2001, the allowed maximum range of the vertical raise of the pavement surface for asphalt concrete pavements is 40 mm, for light pavements and gravel roads with surface dressing 60 mm and for gravel pavements 100 mm. In such seasonal frost regions where temperatures fluctuate much around 0 °C in late autumn/early winter and the yearly average temperature is around +5 °C the amount of rainfall usually exceeds evaporation. That leads to higher moisture content in the soil and also in the road embankment, resulting in a weakening of the load bearing capacity during the period when the road structure is not yet frozen and the subsequent promotion of frost heave during the freezing period. The reduced load bearing capacity and deformations due to frost heave usually lead to traffic restrictions in spring as well as the risk of road pavement surface damage. The effects of uneven frost heave and road pavement

doi:10.3846/bjrbe.2014.28

surface damages affect considerably traffic safety and driving comfort which also has an economical effect both to the road users and road maintenance.

Frost heave assessment of roads can be conducted by using geometric levelling (e.g. Aavik *et al.* 2013). The work usually includes profile-wise embedding permanent benchmarks with pre-defined intervals in the longitudinal direction of the pavement surface of the road and then conducting surveys at certain time-epochs (Mroczkowski 2009). The levelling results illustrate the vertical displacements of the road surface but the data have relatively poor spatial resolution (several tens of meters). Alternatively, the effects of frost heave can be assessed by using mobile terrestrial laser scanning (MTLS) and ground penetrating radar (GPR) see e.g. Peltoniemi-Taivalkoski and Saarenketo (2012). MTLS and GPR are cost effective and better suited for analyzing longer road sections (e.g. Thodesen *et al.* 2012). The MTLS accuracy however, is normally no better than 10 mm due to complexity of height determination by combining Global Navigation Satellite System (GNSS) and Inertial Measurement Unit (IMU) data. To overcome the problems of data generalization in levelling and aiming at observing shorter sections of roads with accuracies better than 10 mm this study tests novel TLS technology for assessing the frost heave induced vertical displacements. To our present knowledge no other studies on the usage of TLS for determining the occurrence and the extent of road frost heave have been published, yet. In addition, also the TLS economic viability and accuracy for this task is discussed. The used methods and results with key features are described as follows. The introduction is followed by explanation of causes of road deformations. The third section gives an overview of geodetic monitoring technology. The fourth section describes the case study, design of the deformation monitoring, establishing the reference network, TLS data acquisition. The data post processing procedures are described briefly in the fifth section. The frost heave results in a test road are presented in the sixth section. Conclusions and discussions conclude the paper.

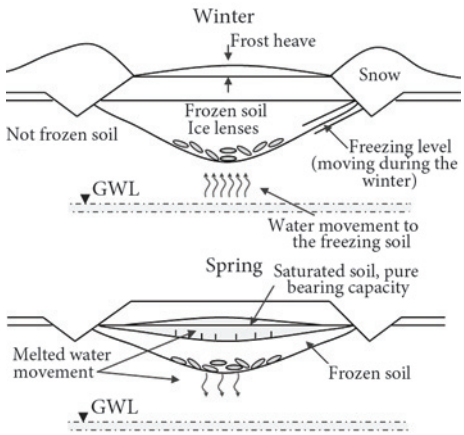

Fig. 1. Frost heave formation in winter (upper figure) and thawing process in spring (lower figure) (Rahiala *et al.* 1988). GWL denotes ground water level

2. Causes of deformations of roads

Road surfaces are subjected to continuous stress of unbalanced loads caused by vehicles moving on it. The main role of the road pavement is to bear the loads originating directly from the wheels of vehicles and distribute them to the embankment, which withstands the stresses caused by the traffic load. Pavement distortions may in part be attributed to human-made mistakes at road construction, such as the use of inappropriate materials, making a layer too thin or leaving out a layer, insufficient compaction, etc. (Mroczkowski 2009).

However, it is the unbalanced deformation of the embankment that has the most adverse influence on the pavement surface shape. According to Mroczkowski (2009) the most common causes of such a deformation include:

– geological diversity of the embankment;

– embankment movements caused by soil loss due to a faulty drainage system, incorrect support of slopes;

– an existing road failing to provide adequate support of the earthwork;

– ground movement connected with desiccation by trees;

– contractions or expansions of an argillaceous bed connected with the embankment's moisture content;

– a change of the ground water level caused by floods, draining or irrigation works.

The main factors underlying the seasonal climatic influence on the road structure are temperature fluctuations, moisture and freezing conditions. Three factors lead to the formation of frost heave: *(i)* soil that is frost-susceptible, *(ii)* a freezing depth that reaches the soil, *(iii)* the presence of moisture (water) in the soil (high ground water level). If one of the factors is missing, the frost heave will not appear or will be limited.

The freezing of the road structure is divided into two phases: first, simple freezing, when the pavement is beginning to freeze and the freezing depth is gradually increasing; second, frost heave formation, when the soil is beginning to freeze, leading to the increase of its volume due to the expansion of frozen water and formation of ice lenses, leading finally to the rising of the pavement surface (Fig. 1).

During the spring the thawing process starts from the top of the pavement. At the same time the lower parts of the pavement and sub-base soil are still frozen. As a result, melted water does not have the possibility to flow out of the pavement structure, and the load-bearing capacity of the saturated structure decreases causing pavement deterioration (cracking, crazing, and rutting) under the traffic load (Fig. 1). Frost heave will disappear after the soil embedded ice has melted.

Frost heave may yield longitudinal cracks in the middle of the roadway (Fig. 2). However, frost heave induced cracks can appear also in other areas of the pavement. Those cracks can occur due to irregularities in the road structure. Road structures are traditionally constructed in layers and each soil/material used in corresponding layer has to have homogenous properties across the whole transverse and longitudinal profile of the road. In the case

of inhomogeneous properties of the layer (e.g. due to different soil/material types are used in the same layer), those layers due to their different clay and silt content can behave differently during freezing and thus can cause variable magnitude of the frost heave on the pavement surface, which will lead to the appearance of cracks on the transitional area of soil/material properties.

Some of these conditions, which result in the occurrence of frost heave can be determined and eliminated during the reconstruction design of an existing road using geodetic methods described below.

3. Review of geodetic monitoring technology

This section gives an overview of two different techniques to acquire height information of a road pavement surface. Traditionally for road deformation monitoring solely geometric levelling has been used for determining the heights of pre-installed deformation benchmarks in the pavement. Using just levelling in such application is relatively time-consuming, especially in cases of large number of deformation survey points. Novel TLS technology, however, enables to acquire a large (up to millions) number of points within seconds. Though levelling is time-consuming it has yet no alternative for sub-mm accurate height determination. This case study uses geometric levelling for height reference and for verifying deformation monitoring results obtained by the TLS technology.

3.1. Geometric levelling

Geometric levelling is the most precise method for obtaining elevations of ground points. In geometric levelling the height difference between two points is determined by the differences of the levelling staff (placed on top of the involved points) readings.

In deformation monitoring an optical levelling instrument with a built-in compensator (with typical standard deviation of 2.0...3.0 mm/km for double run levelling route) can be used. To minimize the possibility of errors by incorrect staff readings, an electronic levelling instrument with a code staff could be used. For fulfilling more rigorous accuracy requirements an optical levelling instrument with a parallel plate micrometer or a precise electronic level with special invar bar staffs should be used in order to achieve accuracy up to 0.3 mm/km for double run levelling route.

For determination of road deformations permanent levelling benchmarks are usually installed in the form of profiles (minimum three points – two at the side of the road and one in the centre) in the longitudinal direction spacing up to a few dozens of meters, depending on resources available.

3.2. Terrestrial laser scanning

In principle TLS operate similarly as reflectorless total stations, which measure simultaneously horizontal and vertical angles and the range to objects of interest without the need of placing a reflector at those points. Nowadays many scanners are equipped with total station-like functions such as centring over a known geodetic reference point, determining the instrument orientation to the backsight target or by calculating the position and the height of the instrument by resection. A detailed overview of TLS technology and orientation methods is given in Alba and Scaioni (2007).

Based on the scanning technology, TLS devices are divided into two types: triangulation scanners and time of flight (TOF) scanners. Whereas triangulation scanners are mainly short-range (< 25 m) devices, nonetheless triangulation scanners have very high accuracies in the order of tenth of millimetres. In terms of working principles TOF scanners apply either the pulse modulation method (also known as the direct time-of-flight method) or the amplitude modulation continuous wave method (AMCW, also known as the phase shift method). In the pulse modulation method the travelling time of a single pulse reflected from the target is measured. Typical pulse modulation laser scanners measure up to 50 000 points/s in ranges up to several hundred meters with the range accuracy of 4 mm to 10 mm. In the amplitude modulation method the phase difference between the sine modulated transmitted and reflected waves are measured. This method allows faster measuring, up to 1 000 000 points/s typically within ranges under 100 m with the range accuracy of 2 mm to 5 mm. Due to decreasing intensity of the amplitude modulated waves the phase shift cannot be reliably detected for longer ranges.

In general, the TLS instruments are optimized for a fast and automated data acquisition in ranges typically from one to few hundreds of meters. The acquired data forms a point cloud of n observations where each point holds 3D coordinates (x_i, y_i, z_i), $i = 1, \ldots, n$ in the scanner's intrinsic coordinate system, provided that the scanner's axes (vertical and horizontal axis) are perfectly aligned. The scanners intrinsic coordinates of the survey points are computed from the measured spherical polar coordinates as follows:

$$\begin{bmatrix} x_i \\ y_i \\ z_i \end{bmatrix} = \begin{bmatrix} \rho_i \sin\varphi_i \sin\theta_i \\ \rho_i \sin\varphi_i \cos\theta_i \\ \rho_i \cos\varphi_i \end{bmatrix}, \quad (1)$$

where θ_i – the horizontal angle with respect to initial direction; φ_i – is the zenith angle; ρ_i – the slope distance from the scanner to the object surface.

The scanned data points are tagged also with an uncalibrated intensity (I) value of the reflected signal. In addition, scanners equipped with a digital photo camera enable to assign the RGB values to survey points during the post-processing. Thus an i-th TLS survey point is characterized by the following data string:

$$\left\{\left(x_i, y_i, z_i, I(x_i, y_i, z_i), RGB(x_i, y_i, z_i)\right), i = 1,...,n\right\}, \quad (2)$$

where x_i, y_i, z_i – the coordinates, $I(x_i, y_i, z_i)$ is the intensity; $RGB(x_i, y_i, z_i)$ – the colour code.

The transformation of the intrinsic coordinates (x_i, y_i, z_i), $i = 1, \ldots, n$ of an individual i-th survey point into extrinsic (e.g. national) coordinate system (x_i^E, y_i^E, z_i^E), $i = 1, \ldots, n$ (also known as georeferencing) is described as follows:

$$\begin{bmatrix} x_i^E \\ y_i^E \\ z_i^E \end{bmatrix} = \begin{bmatrix} x_S^E \\ y_S^E \\ z_S^E \end{bmatrix} + \mathbf{R}_3(\kappa)\mathbf{R}_2(\phi)\mathbf{R}_1(\omega) \begin{bmatrix} x_i \\ y_i \\ z_i \end{bmatrix}, \quad (3)$$

where (x_S^E, y_S^E, z_S^E) – the coordinates of the centre of the laser scanner expressed in the extrinsic system. $\mathbf{R}_1(\omega)$, $\mathbf{R}_2(\phi)$, $\mathbf{R}_3(\kappa)$ are the matrices for rotation around the *x*-, *y*- and *z*-axes respectively; (ω, ϕ, κ) are the rotation angles (from the scanners intrinsic coordinate system into extrinsic coordinate system) about the *x*-, *y*- and *z*-coordinate axes, respectively:

$$\mathbf{R}_1(\omega) = \begin{bmatrix} 1 & 0 & 0 \\ 0 & \cos\omega & \sin\omega \\ 0 & -\sin\omega & \cos\omega \end{bmatrix}, \quad (4)$$

$$\mathbf{R}_2(\phi) = \begin{bmatrix} \cos\phi & 0 & -\sin\phi \\ 0 & 1 & 0 \\ \sin\phi & 0 & \cos\phi \end{bmatrix}, \quad (5)$$

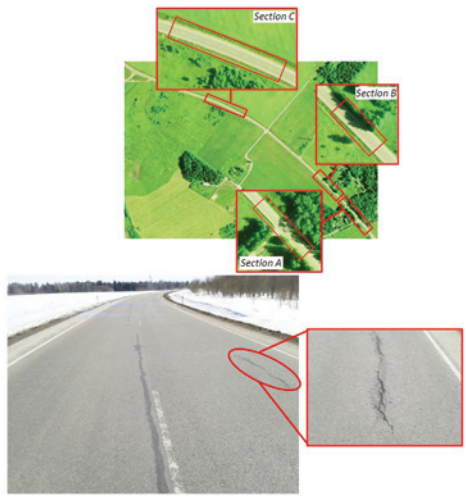

Fig. 2. Road sections A, B and C (left hand side); note longitudinal cracks in the centre and on a road side at the section C (right hand side)

Table 1. Description of the pavement design

Pavement layer (ordered from top to bottom)	Layer thickness
Top layer. Asphalt concrete (in two layers)	8 cm
Base layer of limestone rubble (fraction 16/32, wedged with fraction 8/12). Also the designer allowed using milled asphalt (not over 2 cm thick) for binding the upper layer of the base	20 cm
Drainage layer, filtration module > 2.0 m (in some cases 3.0 m) per 24 h	Average thickness 24 cm, minimal thickness 20 cm
Bottom layer. Fine sand, filtration module > 1.0 m per 24 h	Minimal 40 cm

$$\mathbf{R}_3(\kappa) = \begin{bmatrix} \cos\kappa & \sin\kappa & 0 \\ -\sin\kappa & \cos\kappa & 0 \\ 0 & 0 & 1 \end{bmatrix}, \quad (6)$$

If the scanner is equipped with a dual-axis compensator, then the instrument's *z*-axis (coincides with the plumb-line) is parallel with the extrinsic system's *z*-axis. In this case the rotation angles ω and ϕ become to zero, i.e. $\mathbf{R}_1$, $\mathbf{R}_2$ in Eq. (3) become equal to the unit matrix. Thus, a turn around the *z*-axis would be sufficient for georeferencing see section 5.

4. The case study

4.1. General description of the test road

The case study includes three road sections on the Vaida-Urge road T-11202, in northern part of Estonia. The road was fully reconstructed in 2008, but already in spring 2010 pavement damages were detected. The pavement had longitudinal cracks mainly in the centre of the road and in some places on the road sides (Fig. 2). Although the cracks were repaired by filling them with bitumen, they have occurred again. The cause of these cracks may be connected with the road's last reconstruction. The road had been widened without removing the existing embankment. The cracks emerged at the transition boundaries between the existing embankment layers and the new ones. The major negative influence to the road pavement is also the relatively high level of ground water level, primarily within the A and B sections. Obviously, this in conjunction with non-compatible materials contributes to the effects of frost heave. Frost heave is expected, since Estonia lies in the seasonal frost region, where the frost season begins in late November and ends in April. The average temperature in February, the coldest month, is usually around –5 °C, in some periods within the winter season far below zero, about –20 °C or even lower. According to the Estonian Environment Agency the average temperature for the entire 2012/2013 winter season was –5 °C, which is somewhat colder than the seasonal average (–3 °C). Due to the fact that roads are kept free of snow during the entire winter, according to *Elastsete teekatendite projekteerimise juhend (Guide for the Design of Elastic Pavements)* issued by the *Estonian Road Administration* in 2001 the depth of embankment freezing could reach to the depth of 1.25 m.

The road design followed the class IV road parameters, which are based on a 43 standard axle load (100 kN) frequency per 24 h as defined by the regulation *Tee projekteerimise normid ja nõuded (Standards and requirements for road design in Estonia)*, the class IV road parameters, which are based on a 43 standard axle load (100 kN) frequency per 24 h. The description of the designed pavement is reviewed in Table 1.

4.2. Overview of the road conditions

Presumably, the cracks in sections A and B are mainly caused by frost heave. The load bearing capacity of sections A and B were tested using a falling weight deflectometer

(FWD). The load test results were compared with the results of tests on other parts of the same road. The comparison showed that sections A and B had the lowest load bearing capacity values. According to a technical report by *Sillamäe, S. 2013. T-11202 Vaida-Urge tee defektide põhjuste kindlakstegemine (T-11202 Vaida-Urge Road the Identification of Causes of Defects in the Road)*, the elasticity modulus of the A and B sections was 220 MPa, while the average elasticity modulus for the other sections was in average 253 MPa. Recall that the load bearing capacity of a road is affected by various factors, such as the type of sub-soil, soil moisture content, embankment layer material used, etc. The road sections A and B had shallow ditches, whereas the area near the road was covered with hydrophytic plants. The conditions thus indicate a soil with high moisture content.

The C section of the road is superelevated due to its location at a curve. The cracks in the pavement may be the result of different factors, such as pavement creep deformation, slope creep or frost heave. The core samples taken from the C road section indicate the usage of gravelly clayey sands (fine particle content approx 30% only) instead of fine sand, as prescribed by the reconstruction design instructions. Gravelly clayey sand exhibits less adhesion than fine sand, thus allowing the occurrence of creep deformation. Therefore, the upper layer of the surface of the embankment may have deformed due to traffic load, thus leading to the formation of cracks. It is also likely that due to the poor filtration module of the sand, the moisture content in that layer has contributed to occurrence of frost heave.

4.3. Design of the deformation monitoring

This section reviews the applied geodetic monitoring procedures. First, height reference for the road deformation monitoring was established and measured before the road surface scannings. These were carried out in two epochs:

– at the above zero temperatures in November 2012 (fall);

– at the time of expected frost heave maximum during the snow thawing period in April 2013 (spring).

The aim of this work is to assess the range and spatial distribution of frost heave with sub-centimetre accuracy using TLS technology.

4.3.1. Establishment of the height reference

The height reference for the frost heave (ΔH_{heave}) assessment was established using geometric levelling.

The height reference consisted of five benchmarks embedded into the surface of the road pavement (Fig. 3). The height reference was connected to a single geodetic reference point no 324, the normal height of which is known. The centre of this geodetic point is a 0.77 m long steel rod with a cone-shaped anchor at the bottom. The top of the reference point is approx 0.25–0.30 m below the ground surface (Fig. 4).

The double-run geometric levelling was proceeded with an electronic level Leica Sprinter 100 (allowing for height determination standard deviation as of 2.0 mm/km) with two standard aluminium staffs. The forth and back sights during the levelling were kept equal and two readings were taken at each staff.

The disclosures of the 1.15 km long closed (forth and back) levelling route were +0.0124 m and –0.0012 m, for fall and spring measurements, respectively. These disclosures were further adjusted. Thus, the heights of the reference points are sufficiently accurate for achieving the aim of the work.

The heights of the reference points indicate an overall rise of the pavement surface with respect to the initial geodetic point. The maximum rise is +0.0621 m (cf. Table 2).

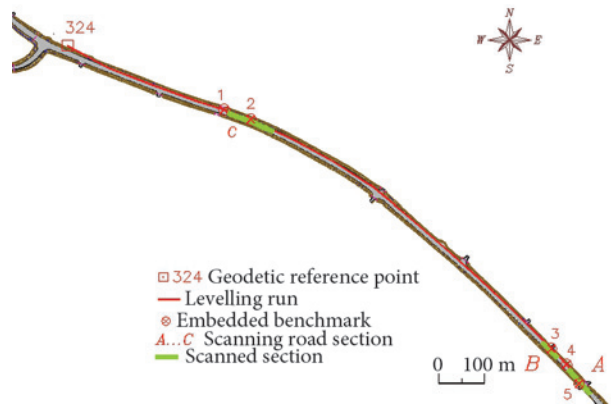

Fig. 3. Locations of the scanned areas (depicted in green) and the levelling benchmarks. Section A was scanned from benchmark 5; section B was scanned from benchmark 3; section C was scanned from benchmark 2; benchmarks 4 and 1 were used as targets for the orientation of the scans

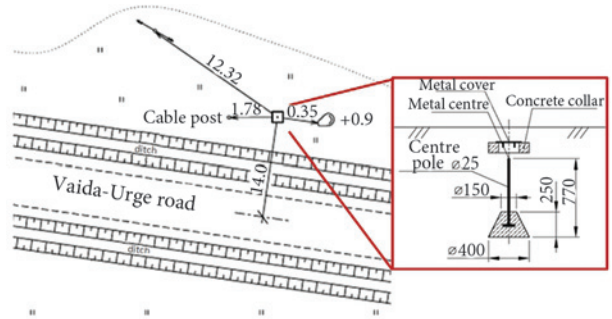

Fig. 4. Location and the design of the used initial geodetic point (*Riigi Maa-amet 2013. Geodeetiliste punktide andmekogu kaardirakendus [*Estonian Land Board. Geodetic Data Map Application])

Table 2. The levelled heights of embedded benchmarks with respect to the used initial geodetic point

Benchmark number	Results in fall 2012, m	Results in spring 2013, m	Differences (i.e. the frost heave): spring minus fall, m
1	48.1062	48.1402	+0.0340
2	48.4046	48.4150	+0.0104
3	50.9743	51.0200	+0.0457
4	50.9955	51.0354	+0.0399
5	50.9752	51.0373	+0.0621

The geometric levelling results will be used as references for TLS survey and to verify the accuracy of TLS results of this study. Verifications of the TLS accuracy at roadworks by total station surveying have earlier been studied, e.g. by Mill *et al.* (2011). The stability of the initial geodetic point (no. 324) was not specially verified. Therefore there is a mild risk of the geodetic point to rise due to frost heave as well since the point is at the depth of only in about one meter in the soil. Note however, that due to thick snow cover in the surroundings of the point during the winter it is unlikely that the frost would reach beneath the geodetic point's anchor. Therefore in further calculations it is assumed that used geodetic point is practically stable.

4.3.2. Terrestrial laser scanning of the road sections

The TLS survey was conducted immediately after levelling of the height reference points. A TOF terrestrial laser scanner Leica ScanStation C10 (equipped with dual-axis compensator) was used for the measurements. The maximum measuring range of the device is 300 m with a 360×270° field of view and maximum scanning rate of up to 50 000 points/s. The range and angle accuracy specifications are ±4 mm and ±12″, respectively. The scanner was erected and centered above the benchmarks 2, 3 and 5. The height of the scanner z_{TLS} with respect to the initial geodetic point is determined as:

$$z_{TLS} = z_b + H_{TLS}, \tag{7}$$

where z_b – the levelled height of the benchmark; H_{TLS} – the tape measured height of the instrument above the benchmark. The spatial resolution for scanning was set to 10 cm at 100 m which defines the vertical and horizontal point spacing on a vertical surface prependicular to the line of sight. The resulting average point density on the (horizontal) road surface was in average approx 12 cm, being less dense at longer distances from scanner.

Fig. 5. Scanning the road section A in April 2013. Note thawing snow along road sides

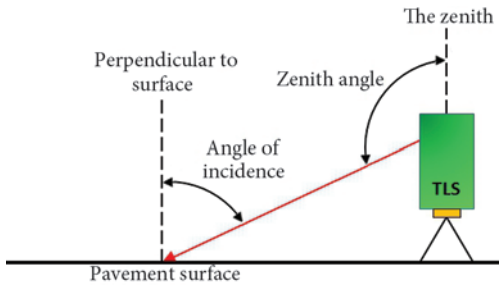

Fig. 6. Angle of incidence at scanning, the red line indicates the laser beam

The first scanning epoch was proceeded in fall. The temperature was +1 °C, the humidity, 98%, and the wind speed, 3 m/s during the measurements. The pavement surface was wet, making the conditions for laser scanning unfavourable due to possible signal attenuation. The second scanning epoch was proceeded in spring. The temperature was +4 °C, the humidity, 33%, and the wind speed, 3 m/s during the measurements. The road was dry, and conditions for scanning were almost ideal, though snow piles still banked the sides of the road. However, the water from the thawing snow prevented data acquisition alongside of the A section, therefore the survey data from the near sides of the pavement (Fig. 5) were excluded from further comparisons.

Lichti (2007) and Soudarissanane *et al.* (2007) suggest that the scanning incidence angle (Fig. 6) should not exceed 65–80°. Soudarissanane *et al.* (2011) states that larger incidence angles result approximately 20% of the signal deterioration. The signal deterioration causes the increase of noise in the point cloud, and therefore yields substantially larger standard deviation values (Soudarissanane *et al.* 2011). Since the scanning object was the horizontal road surface the scanner was erected as high as possible (Table 3, column 2) to minimize incidence angle values. At longer scanning distances the incidence angles neared 90°, though.

At such larger incidence angles the angular precision determines primarily the precision of the height of the scanned points. The law of error propagation is used to compute the precision of the height of the scanned point:

$$\sigma^2(\hat{H}) = \sum_{i=1}^{n} \left(\frac{\partial f}{\partial w_i} \right)^2 \sigma^2_{(w_i)}, \tag{8}$$

where $\sigma^2(\hat{H})$ denotes the variance of the road surface height determined by TLS with respect to the initial geodetic point. Note that $\hat{H}$ is an estimate of the actual height H stemming from the levelling, tape-measured scanner height, the TLS range and angle measurements (Eq (9)), f is the function $H = f(w_i)$, $i = 1, ..., n$, relating the observations (w_i), $i = 1, ..., n$, and the height. The notation $\hat{H}$ represents height in order to distinguish it from the scanner z-coordinate. $\sigma^2_{(w_i)}$ is the error of an i-th observable. The observation equation, i.e. function f, for an i-th scanned road point is written as (Fig. 7, Eqs (1) and (7)):

$$\hat{H}_i = z_b + H_{TLS} + \rho_i \cos\varphi_i, \tag{9}$$

where ρ_i – slope distance from the scanning station to the reflective surface; φ_i – zenith angle; $\hat{H}_i$ – the resulting road surface height. Inserting Eq (9) into Eq (8) and calculating the derivatives the standard uncertainty $\sigma(\hat{H})$ of a survey point height is found as:

$$\sigma(\hat{H}) = \pm\Big[\sigma^2(\hat{z}_b) + \sigma^2(\hat{H}_{TLS}) + (\cos\varphi_i)^2 \cdot \sigma_{dist}{}^2 + \rho_i{}^2 \sin\varphi_i{}^2 \cdot \sigma_{angle}{}^2 \Big]^{\frac{1}{2}}, \tag{10}$$

where $\sigma^2(\hat{z}_b)$ – the estimated uncertainty of the benchmark height determined by levelling (2.0 mm/km by specifications, recall, also, that disclosures of levellings in fall and in spring were + 0.0124 m and – 0.00120 m, respectively, thus, in the worst case scenario the benchmark error could contribute up to 3 mm only); $\sigma^2(\hat{H}_{TLS})$ – the estimated variance of the tape measured height of the instrument (the corresponding error would not exceed 2 mm, at most); σ_{dist} – the scanner's standard distance uncertainty; σ_{angle} – the scanner's standard angular uncertainty. Numerical values for σ_{dist} and σ_{angle} were taken from the manufacturer's specifications (see above). Since $\sigma(\hat{H})$ depends on the distance ρ_i and angle φ_i, then it is individual for each surface point.

The standard uncertainties $\sigma(\hat{H})$ for the road survey points were calculated at four standard locations at 5 m, 10 m, 25 m and 50 m from TLS station (Table 3).

The mean value of standard uncertainties of height $\sigma(\hat{H})$ of the survey points at different locations equals ±4.0 mm (one sigma), which by adopting the 95% confidence interval level (two sigma) yields an uncertainty of ±8.0 mm. Thus the uncertainty of two compared data sets (fall and spring) equals to $8.0\sqrt{2} = \pm 11.3$ mm. Hence, height differences exceeding ±11.3 mm between two TLS epochs at a location is considered as actual deformation (Fig. 7).

4.4. Verification of the TLS survey heights

When scanning the road sections (both in fall and spring) a specially designed 7.62×7.62 cm HDS (High Definition Survey) target was placed onto one of the embedded benchmarks (Fig. 7). A target was scanned from each TLS station. Since the height of the target above the benchmarks was measured, then this allowed determining the benchmark height from the TLS data. The TLS results are then compared with levelled results and the corresponding discrepancies are presented in Table 4. Larger discrepancies (in road section A) are associated with the target on the benchmark number 4 (Table 4). The discrepancies are likely either due to non-verticality of the target or measuring the target height or scanning the targets or a combination of aforementioned errors. The RMS-error value as of ±2.9 mm was calculated by using all discrepancies in the last column of Table 4.

The resulting RMS uncertainty value agrees reasonably with the theoretical TLS uncertainty (section 4.3.2.). The actual discrepancies differ from the estimated one (8.0 mm, at 95% confidence interval level) by 5.1 mm. The latter indicates that the achieved uncertainty is substantially better than the theoretical uncertainty (section 4.3.2.).

5. Laser scanning data processing

TLS data processing was divided into two phases. At first, the 3D point cloud was processed by using commercial Leica Cyclone 8.0 software, where information outside the object of interest was removed and 3D TIN models of the road sections were created and compared. Second, the Autodesk AutoCAD Civil 3D 2013 software was used to analyse the results (see section 6).

The laser scannings were proceeded in an arbitrary coordinate system. For the fall and spring TLS surveys the origins of the *x* and *y* coordinates coincided exactly (recall, that in both occasions the scanner was centred above the same benchmark). However, the directions of coordinate (*x*, *y*) axis were shifted with respect to each other. The orientation

Table 3. Height uncertainties at four standard locations

Point number	Height of the TLS H_{TLS}, m	Slope distance ρ, m	Zenith angle φ, ° ,	Standard uncertainties $\sigma(\hat{H})$, m
1	2.0	5	111°48'	0.0039
2	2.0	10	101°19'	0.0037
3	2.0	25	94°34'	0.0039
4	2.0	50	92°17'	0.0046

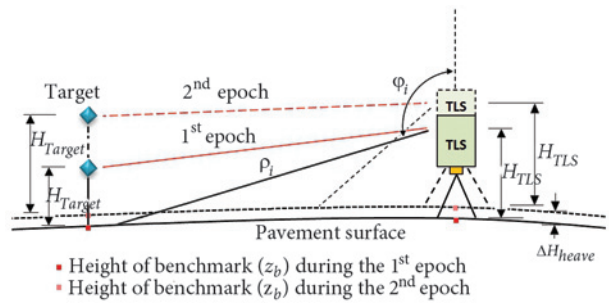

Fig. 7. Scanning of a road section in two epochs, the red and black lines indicate the laser beams reflecting back from targets and from the road surface, respectively. The used symbols are explained in the text

Table 4. Heights of the benchmarks obtained from TLS data and levelling

Road section	Epoch	Benchmark number	Height of target H_{Target}, m	Heights from TLS data in m, reduced from the target centre	Heights from levelling in m, source Table 2	Discrepancies, m
A	fall	4	1.900	50.989	50.995	–0.006
	spring	4	1.900	51.036	51.035	+0.001
B	fall	4	0.700	50.997	50.995	+0.002
	spring	4	1.900	51.032	51.035	–0.003
C	fall	1	0.700	48.106	48.106	+0.000
	spring	1	0.200	48.140	48.140	+0.000

of the coordinate axis of the point clouds were conducted at the post processing in Leica Cyclone. First, the point cloud's *x*-axis was defined by the scanner location and the target placed above one of the benchmarks (Fig. 8). Thereafter the benchmark-target direction (denoted as *x*' in Fig. 8) of the fall measurements was rotated (around the *z*-axis) to coincide with the post processing *x*-axis. Then the benchmark-target direction (denoted as *x*" axis in Fig. 8) of the spring measurements was rotated (around the *z*-axis) to coincide with the post processing *x*-axis as well. Such an orientation

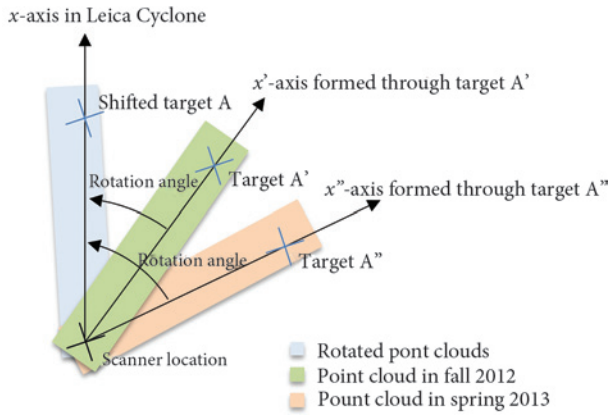

Fig. 8. Merging the fall and spring TLS data through the TLS-target direction. Point clouds of the fall and the spring TLS data are rotated around *z*-axis using benchmark-target direction. View from the top

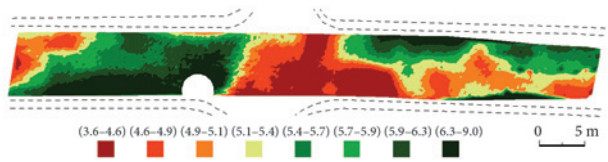

Fig. 9. Frost heave in the road section A in spring 2013. Length of the section 63 m, the non-coloured half-circle indicates the location of the scanner, dashed lines denote roughly the edges of tarmac and the widths of road shoulders, the colour ranges are in cm

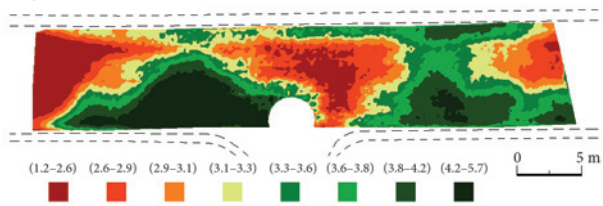

Fig. 10. Frost heave in the road section B in spring 2013. Length of the section 42 m, the circle indicates the location of the scanner, dashed lines denote roughly the edges of tarmac and the widths of road shoulders, colour ranges are in cm

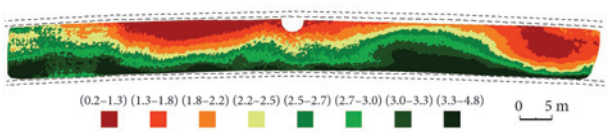

Fig. 11. Frost heave in the road section C in spring 2013. Length of the section 94 m, the non-coloured half-circle indicates the location of the scanner, dashed lines denote roughly the edges of tarmac and the widths of road shoulders, colour ranges are in cm

method was applied to all sections. The heights of point clouds were 1D corrected by the H_{TLS} differences (Fig. 7) in the fall and spring measurements.

The laser-point based centring accuracy of the scanner was estimated to be around ±1.0 mm. Such centring error has no considerable effects on the results of the study, recall also an average data resolution of approximately 12 cm. Noise from passing cars and other commuters on the surface of the road was removed using an algorithm of smooth surface which segments the points representing the smooth surface from the point cloud. Followed by noise removal 3D TIN models of the road sections were created and compared. The results of the comparison were exported into .txt format and imported into Autodesk AutoCad Civil 3D.

6. Results of frost heave assessment

The surface comparison results were analysed in Autodesk AutoCad Civil 3D by creating comparison surfaces using the imported data-points. The comparison surfaces show height discrepancies from different epochs using eight ranges of colours from dark green to dark red.

Results for road section A indicate clearly the effects of uneven frost heave (Fig. 9) with a minimum surface rise of +3.6 cm in the centre of the road (dark red) and a maximum rise of +9.0 cm at the sides of the road (dark green). The total area investigated was 425.7 m². The greater part of the total area, that is 50%, had risen in the range of +5.1 cm to +6.3 cm; 37% of the area had risen in the range of +3.6 cm to +5.1 cm; and 12% of the area had risen in the range of +6.3 cm to +9.0 cm. The extreme rise of +9.0 cm is only within an area that is less that 1%. This might be caused possibly by an erratic point.

Results from road section B also indicate the effects of uneven frost heave (Fig. 10) with a minimum surface rise of +1.2 cm in the centre of the road and at the left end (dark red) and a maximum rise of +5.7 cm at the sides of the road (dark green). The total area investigated was 311.6 m². Results show that 50% of the total area had risen in the range of +3.1 cm to +4.2 cm; 37% of the area had risen in the range of +1.2 cm to +3.1 cm; and 13% of the area had risen in the range of +4.1 cm to +5.7 cm.

Results from road section C indicate frost heave (Fig. 11) with a minimal surface rise of +0.2 cm on the higher side of the slope (dark red) and a maximum rise of +4.8 cm at the centre of the curve on the lower side of the slope (dark green). The total area investigated was 720.0 m². The results show that 38% of the area had risen in the range of +2.2 cm to +3.0 cm; 37% of the area had risen in the range of +0.2 cm to +2.2 cm; and 25% of the area had risen in the range of +3.0 cm to +4.8 cm.

The results of the laser scanning show vertical deformations up to +9.0 cm on section A, up to +5.7 cm on section B, and up to +4.8 cm on section C. The results obtained clearly indicate frost heave. The study revealed that the frost heave was spread across the road surface in an uneven manner, which is considered an unacceptable behaviour.

Though the incidence angles at scanning were nearing 90°, they do not appear to affect significantly the

results, since the resulting surfaces were regular over all road sections.

7. Conclusions and discussions

This contribution presented the methodology for collecting and processing data for the purpose of determining magnitudes and spatial distribution of frost heave by terrestrial laser scanning. The data collecting methodology combines the geodetic methods of geometric levelling and terrestrial laser scanning. A complete description of the work carried out on the observed road sections is presented, including the establishment of the height reference, terrestrial laser scanning data acquisition, data processing and the creation of the analyse surfaces. The achieved root mean square error was by verification in fall ±2.9 mm, where the assumed accuracy was ±8.0 mm on 95% confidence interval level.

It is difficult and even impossible to provide such high-resolution results by conventional survey methods such as total station survey or geometric levelling thus the ability to detect spatial distribution of frost heave makes laser scanning an effective and attractive tool. The fact that the concerned areas are relatively limited makes the use of terrestrial laser scanning, which by nature is static, cost effective due to its ability to acquire a relatively large amount of data in a short period of time without disruption to traffic.

Problems with terrestrial laser scanning might occur when scanning at below 0 °C temperatures. Although in general such scanners are able operating in mild cold, the accuracy specifications provided by the manufacturers are determined in temperatures above 0 °C, therefore the accuracy of scanning in temperatures below zero is not guaranteed. Another problem with terrestrial laser scanning (and this applies to mobile terrestrial laser scanning as well) is the problem with rubble or debris, even snow on the road surface will distort the acquired data. Using conventional surveying technology such as total station survey or levelling it is possible to eliminate such potential distortions. However the conventional surveying technology has a lower productivity compared to terrestrial or mobile terrestrial laser scanning.

Nevertheless, for future projects it is advisable that terrestrial laser scanning surveys should be accompanied with verifying observations by other geodetic technologies.

A useful benefit of using terrestrial laser scanning surveying in road survey projects would also be the possibility to monitor the road during the guarantee period following construction to verify the quality and stability of the road pavement. In addition, it is also advisable to use terrestrial laser scanning to determine frost heave sensitive areas of the existing road embankment in the pre-reconstruction stage. Determining frost heave sensitive areas in the pre-reconstruction stage would help preclude possible reconstruction design flaws.

Acknowledgements

The Estonian Road Administration is thanked for allowing using the geodetic monitoring data. The used TLS Leica ScanStation C-10 and the licensed 3D Point Cloud Processing Software Leica Cyclone is purchased within frames of the Estonian Research Infrastructures Roadmap object Estonian Environmental Observatory (funding source 3.2.0304.11-0395, project No. AR12019). Part of this research is supported by the Estonian Environmental Technology R&D Programme KESTA research project ERMAS AR12052.

References

Aavik, A.; Ellmann, A.; Paabo, P. 2013. Use of Geosynthetics for Roadbase Strengthening – Case Study in Swampy Area, in *The XXVII International Baltic Road Conference*. August 26–28, 2013, Vilnius, Lithuania [cited 12 March 2014]. Available from Internet <http://www.balticroads.org/downloads/28BRC/009_T03.pdf>.

Alba, M.; Scaioni, M. 2007. Comparison of Techniques for Terrestrial Laser Scanner Data Georeferencing Applied to 3-D Modeling of Cultural Heritage, in *Proc. of the 3D-ARCH 2007: "Virtual Reconstruction and Visualization of Complex Architectures"*, XXXVI-5/W47. July 12–13, 2007, Zurich, Switzerland [cited 20 June 2013]. Available from Internet <http://www.isprs.org/proceedings/XXXVI/5-W47/pdf/alba_scaioni.pdf>.

Lichti, D. D. 2007. Error Modelling, Calibration and Analysis of an AM–CW Terrestrial Laser Scanner System, *ISPRS Journal of Photogrammetry and Remote Sensing* 61(5): 307–324. http://dx.doi.org/10.1016/j.isprsjprs.2006.10.004

Lichti, D. D. 2010. Terrestrial Laser Scanner Self-Calibration: Correlation Sources and Their Mitigation, *ISPRS Journal of Photogrammetry and Remote Sensing* 65: 93–102. http://dx.doi.org/10.1016/j.isprsjprs.2009.09.002

Mill, T.; Ellmann, A.; Uueküla, K.; Joala, V. 2011. Road Surface Surveying Using Terrestrial Laser Scanner and Total Station Technologies, in *Proc. of 8th International Conference Environmental Engineering*. Ed. by Čygas, D.; Froehner, K. D. May 19–20, 2011 Vilnius, Lithuania. Vilnius: Technika. 1142–1147.

Mroczkowski, K. 2009. Determining Deformation on the Road Surface, in *Proc. of the IX Konferencja Naukowo-Techniczna „Aktualne problemy w geodezji inżynieryjnej"*. March 30–31, 2009, Warsaw, Poland [cited 7 October 2013]. Available from Internet <http://yadda.icm.edu.pl/baztech/element/bwmeta1.element.baztech-article-PWAB-0005-0012/c/httpwww_rog_gik_pw_edu_plphocadownloadnr8732.pdf>.

Paeglītis, A.; Paeglītis, A.; Vītiņa, I.; Igaune, S. 2013. Study and Renovation of Historical Masonry Arch Bridge, *The Baltic Journal of Road and Bridge Engineering* 8(1): 32–39. http://dx.doi.org/10.3846/bjrbe.2013.05

Peltoniemi-Taivalkoski, A.; Saarenketo, T. 2012. *Drainage Maintenance Follow Up – Experiences from the Rouvaniemi and Kittilä Projects, Finland* [cited 15 September 2013]. Available from Internet <http://www.roadex.org/uploads/publications/drainage/ROADEX_IV_Drainage Maintenance Follow Up Finland.pdf>.

Rahiala, J.; Rakennusaineteollisuusyhdistys; Tie- ja vesirakennushallitus; Betonitieprojekti. 1988. *Maabetoni ja betonipäällysteet: ... käytössä maailmalla, sopivatko Suomeen?* ... [Rahiala, J.; Building Materials Industry Association; the Board of Directors of Civil Engineering; Concrete Project.

Land Concrete and Concrete Coating: ... Used in the World, Whether the Finland?]. (Vol. 275 p.). Turku: Tie- ja vesirakennushallitus. ISBN 951-47-1603-5.

Reshetyuk, Y. 2009. *Self-Calibration and Direct Georeferencing in Terrestrial*: PhD Thesis 978-91-85539-34-5. Stockholm: Kungliga Tekniska högskolan [Royal Institute of Technology]. Universitetsservice US AB [cited 15 January 2010]. Available from Internet < http://kth.diva-portal.org/smash/record.jsf?pid=diva2:139761>.

Reshetyuk, Y. 2010. A Unified Approach to Self-Calibration of Terrestrial Laser Scanners, *ISPRS Journal of Photogrammetry and Remote Sensing* 65(5): 445–456. http://dx.doi.org/10.1016/j.isprsjprs.2010.05.005

Riveiroa, B.; González-Jorgeb, H.; Varelab, M.; Jaureguic, D. 2013. Validation of Terrestrial Laser Scanning and Photogrammetry Techniques, *Measurement* 46(1): 784–794. http://dx.doi.org/10.1016/j.measurement.2012.09.018

Soudarissanane, S.; Lindenbergh, R.; Menenti, M.; Teunissen, P. 2011. Scanning Geometry: Influencing Factor on the Quality of Terrestrial Laser Scanning Points, *ISPRS Journal of Photogrammetry and Remote Sensing* 66(4): 389–399. http://dx.doi.org/10.1016/j.isprsjprs.2011.01.005

Soudarissanane, S.; van Ree, J.; Bucksch, A.; Lindenbergh, R. 2007. Error Budget of Terrestrial Laser Scanning: Infuence of the Incidence Angle on the Scan Quality, in *Proc. of the 3D-NordOst 2007*. September 6–7, 2007, Berlin, Germany. [cited 1 June 2013]. Available from Internet <http://citeseerx.ist.psu.edu/viewdoc/download?doi=10.1.1.149.5378&rep=rep1&type=pdf>.

Thodesen, C. C.; Lerfald, O.; Hoff, I. 2012. Review of Asphalt Pavement Evaluation Methods and Current Appilications in Norway, *The Baltic Journal of Road and Bridge Engineering* 7(4): 246–252. http://dx.doi.org/10.3846/bjrbe.2012.33

Tsakiri, M. L.; Pfeifer, N. 2006. Terrestrial Laser Scanning for Deformation Monitoring, in *Proc. of the 12th FIG Symposium on Deformation Measurement and 3rd IAG Symposium on Geodesy for Geotechnical and Structural Engineering*. May 22–24, 2006, Baden, Austria [cited 3 April 2013]. Available from Internet <http://www.ipf.tuwien.ac.at/np/Publications/tsakiriLichtiPfeifer_FIG.pdf> .

Vosselman, G.; Maas, H.-G. 2009. *Airborne and Terrestrial Laser Scanning*. Dunbeath: Whittles publisher. 320 p. ISBN 978-1439827987.

Zogg, H.-M.; Ingensand, H. 2008. Terrestrial Laser Scanning for Deformation Monitoring – Load Tests on the Felsenau Viaduct (CH), in *Proc. of the XXIst ISPRS Congress*. July 3–11, 2008, Beijing, China.[cited 15 June 2013]. Available from Internet <http://www.isprs.org/congresses/beijing2008>.

Received 23 April 2014; accepted 10 June 2014